Received February 20, 2019, accepted March 2, 2019, date of publication March 5, 2019, date of current version March 25, 2019.

Digital Object Identifier 10.1109/ACCESS.2019.2903198

Versatile Conical Conformal Array Antenna Based on Implementation of Independent and Endfire Radiation for UAV Applications

HONGCHENG XU[1], JIANLI CUI[2], JUNPING DUAN[1], BINZHEN ZHANG[1], AND YING TIAN[3]

[1]Key Laboratory of Instrumentation Science and Dynamic Measurement, Ministry of Education, North University of China, Taiyuan 030051, China
[2]Department of Physics and Electronics, Yuncheng University, Yuncheng 044000, China
[3]Sichuan Aerospace Liaoyuan Science and Technology, Co., Ltd, Chengdu 610000, China

Corresponding author: Binzhen Zhang (zhangbinzhen@nuc.edu.cn)

This work was supported in part by the joint funds from the National Natural Science Foundation of China under Grant U1637212 and Grant 61605177, in part by the National Defense Pre-Research Foundation of China under Grant 61404130402, in part by the Fund for Shanxi 1331 Project Key Subject Construction, in part by the Yuncheng University Doctor Initiation Project under Grant YQ-2018011, and in part by the Science and Technology Innovation Project of Shanxi under Grant 20171109.

ABSTRACT This paper proposed an integrated conical conformal array antenna (CCAA) for versatile application to the unmanned aerial vehicles. The CCAA consists of five flexible linear gradient subarrays with a uniform circumferential arrangement around the conical surface. It is also embedded with a pyramid reflective back-cavity (PRBC) within the conical carrier. The implementation for the three different elements of the linear gradient subarray toward impedance match and high isolation was investigated, and their identity resonant frequency (9.8 GHz) principle was developed and demonstrated. Furthermore, the PRBC was presented to improve the radiation null of the elements. A numerical 5-bit phase shifter manipulating phase difference of 72° was then combined with an 8-way power divider to obtain a fixed beam with a half power bandwidth (HPBW) of less than 24°, which indicated the backward endfire direction ($\theta = 180°$) in terms of three circumferential arrays (R#X). Finally, the measurements with the aid of the designed phase shifter and power divider (model SHPDW4-040140S) were conducted. The experimental results show one omnidirectional coverage (360°) in the H-plane through the switching working mode of the elements with a wide scanning solid angle ($\geqslant$72°) when these elements of the subarray hold an identity resonant frequency and exhibit a uniform performance in the point-to-point communication. The measurements of a narrow HPBW of less than 27.5° and the gain over 10.7 dBi in the endfire direction of the three circumferential arrays show great potential in backward blind space detection simultaneously.

INDEX TERMS Conical conformal array antenna (CCAA), flexible linear gradient array (FLGA), pyramid reflective back-cavity (PRBC), 5-bit phase shifter, power divider, wide solid scanning angle, endfire radiation.

I. INTRODUCTION

Conformal antennas, which are usually flexible and assembled on flying platforms, have received increasing global interest, especially in the areas of high-velocity fighter planes and unmanned aerial vehicles (UAVs) because of their desirable aerodynamic features and favorable low profile [1]–[5]. When wireless terminals deal with complicated multitasks, remote endurance cannot be guaranteed because of the electronic weight and mutual electromagnetic interference (EMI) accentuated by added components. In the absence of a back radar [6] or airborne warning and control system [7], target regions in blind spaces on or behind airplanes cannot be detected by airborne antennas effectively. Small UAVs cannot assemble such an antenna system with bulk mass. Hence, a lightweight and conformal versatile antenna that is wrapped around a curved surface integrally for multitask execution, including communication, detection and display, must be investigated and possibly combined with phased array technology to detect blind spaces successfully.

Most developments in conformal antennas merely focused on arrays on cylindrical [8]–[9], spherical [10]–[11], and

The associate editor coordinating the review of this manuscript and approving it for publication was Haiwen Liu.

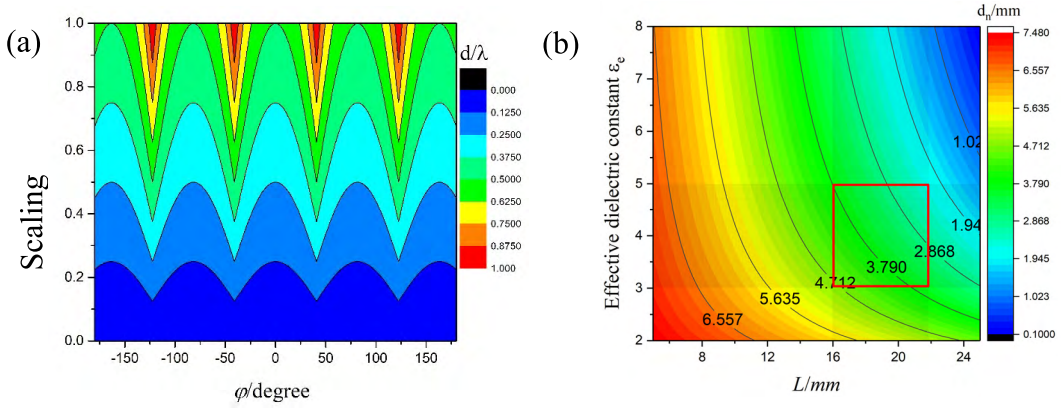

FIGURE 1. Coupling distance and matching position. (a) Relationship between coupling distance and scanning angle. (b) 50 ohm coaxial matching position distance between the feeding port and the patch center with various L and effective dielectric constant.

conical [12]–[14] models, most of which are concentrated solely on single antennas without EMI from the interior of platforms [15]–[18] that omit the arrays uniformity, such as the identity resonant frequency of units, uniform radiation, fixed direction, and same polarization [19]–[21], in favor of reducing EMI and enhancing device efficiency. As a result of the strong mutual coupling of subarrays in proximity space and interior electronic components, antennas are conformal around curved surfaces and are difficult to synthesize with respect to planar arrays with only two dimensions. These restrictions weaken array uniformity, which benefits omnidirectional radiation along the circumferential direction of peripheral arrays [22]. In ensuring a 360° radiation coverage in the H-plane, identity wide-angle radiative elements are arranged on a circular plane to achieve omnidirectional radiation and enable solid-angle scanning instantly. Reconfigurable conformal antennas were proposed in [23] and [24], but these antennas cannot achieve endfire radiation for blind space detection and are thus limited when used in complicated environments [25]–[26]. Achieving a perfect function entails the application of few antennas to achieve multitask implementation. Hence, an interesting research direction is to develop a versatile conical conformal array antenna (CCAA) with wide-angle scanning and endfire radiation.

In this study, the implementation of flexible gradient elements of subarrays was investigated. Based on the model property of a CCAA consisting of five flexible linear gradient subarrays (FLGAs) with an even circumferential arrangement and a pyramid reflective back-cavity (PRBC), conical conformal array radiation patterns were synthesized to obtain the next excited phase of circumferential arrays. Then, the uniformity of the elements was demonstrated in terms of the resonant frequency and omnidirectional radiation features with a wide scanning solid angle. Finally, a 5-bit numerical phase shifter is combined with an 8-way power divider to achieve a fixed beam pointing to the backward endfire direction in the simulation and measurement. The result reveals the potential of the proposed CCCA in versatile UAV detection and communication in a fierce EMI environment.

II. CONFORMAL GRADIENT ARRAY DESIGN METHODS

Flexible array antennas are excellent candidates for high-velocity UVAs. However, keeping all elements of conformal antennas with independent operating ability in a uniform radiation pattern, fixed direction, and same polarization is a major challenge because of the strong interference from complicated feeding networks, the tight coupling of proximity elements on arbitrary curvature, and limited space. In this study, we employ a coaxial probe as the feeding line and a microstrip patch as the element. To collocate the desirable aerodynamics between the flexible antenna and the conical surface, we direct the outline of the gradient patches toward the conic node (Fig. 2). The schematic of the structure shows the operating frequencies of the element denoted as d_n, L_n, and α. α is the arc length of the patch versus the conical surface. Formula (1) is the position disposition of the 50 ohm impedance matching point [27]. In addition, the spacing between the elements determines the effects of mutual coupling acting on the grating lobe and the gain antenna. Formula (2) [28] is the principle behind the limitation of the above factor.

$$d_n = \frac{L_n}{2} - \frac{L}{2}\left(1 - \frac{1}{\sqrt{\varepsilon_e}}\right) \tag{1}$$

$$\frac{d}{\lambda_0} < \frac{k}{1 + |\sin\varphi_m|} \tag{2}$$

where d_n is the coaxial matching position distance between the feeding port and the patch center. L_n is the length of the patch. ε_e is the effective dielectric constant of the multilayer antenna. L is the theoretical length of the patch. $k(< 1)$ is the scaling factor. d is the spacing between the elements. λ_0 is the working wavelength of the antenna (over 9.8 GHz). φ_m is the beam scanning angle.

The characterizations of the mutual coupling and impedance matching position are shown in Figs. 1 (a) and (b),

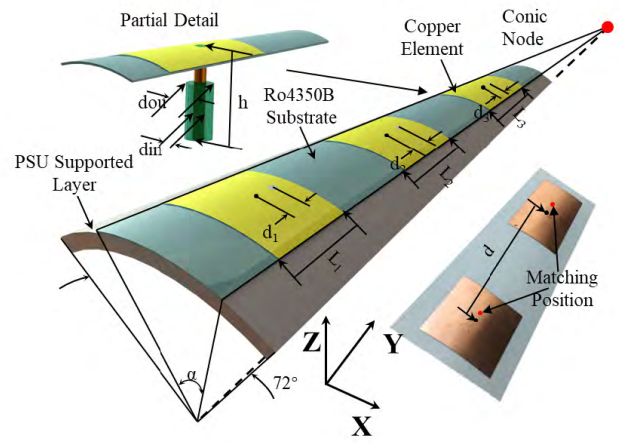

FIGURE 2. Numerical structure of flexible linear subarray around a conical surface.

respectively. The primary cone with a top radius of 0.22 λ_0, bottom radius of 0.9 λ_0, and height of 3.1 λ_0 serves as the antenna carrier.

The relationship between the scanning angle and d/λ0 shows a wide scanning angle leading to a short coupling distance of d < 0.625 λ0. In [28], the coupling distance meets d > 0.5 λ0. As the coaxial matching position distance is related to various L and ε_e, we define a low-cost substrate of Rogers serials materials with a dielectric constant in the range of 3–5 and theoretical patch length of (0.52 λ_0 –0.72 λ_0). This setting restrains the matching distance of d_n within the red frame in Fig. 2 (b). Through a fine adjustment of the value of d_n, three elements operate at identity frequency and lower coupling. From this condition, the final array antenna can be configured in a lower interference and with independent radiation properties.

A. FLEXIBLE LINEAR GRADIENT ARRAY DESIGN

Before the investigation of the CCAA, the electromagnetic performance of the FLGAs must be studied. The FLGA consists of three elements arranged along the generatrix of a cone, as illustrated in Fig. 2. The feeding line comprises one coaxial probe with a copper-inner height of *h* (6.25 mm) and diameter of *din* (1.35 mm). The outer electric substrate is a vacuum cylinder with a diameter of *dou* (1.5 mm). The array- supported layer and antenna substrate are made of polysulfon (PSU, $\varepsilon_r = 3.5$, $\tan\delta = 0.01$) with a 3mm thickness and ultra-thin Rogers 4350B ($\varepsilon_r = 3.66$, $\tan\delta = 0.004$) with a 10 mm thickness (0.008 λ_0), respectively. The distance between two patch centers is *d,* and their physical matching position is shown as a partial detail of the prototype structure. The patches from the bottom to top are labeled as elements 1–3, and the distances between the elements and the bottom edge of the antenna-supported layer are 10, 40, and 64 mm, respectively. The back of the PSU sputter fully covered with copper foil with a thickness of 17 μm is a flexible plate. Through the analysis of part II, we find that the key to acquiring the same operating frequency and independent radiation property is to modify the matching position of the ports and element's arc length.

B. SYNTHESIS OF SAME RESONANT FREQUENCY

The resonant frequency related to matching position and patch arc length is investigated, as shown in Figs. 3 (a) and (b), with the aid of the electromagnetic software Ansys Electronic 18.0. The lengths of three elements (1–3) are 18, 16.4, and 17, respectively. Each resonant point forms a deflection versus the eccentricity of $d_n = 0$ mm as the resonant frequency reaches its peak value. The negative correlation between the resonant frequency and the matching distance is exhibited in Fig. 3(a).

The gradient of the resonant frequency for element 3 is greater than that for elements 1 and 2. This result indicates that a small patch-3 is easily made susceptible by matching position. In the figure, gray A denotes the same operating frequency zone (9.34 GHz, 9.83 GHz), in which the identity resonant frequency can be simultaneously achieved with increasing d_n. In addition, all elements' resonant frequencies present a negative correlation with the increase in patch arc length, as shown in Fig. 3(b), when $d_1 = 0$ mm, $d_2 = 0$ mm, and $d_3 = 2$ mm. Owing to the small radius of the top element, that is, the cone profile, the uniform arc length determines a short patch bottom edge and thus cause a small rate of change for element 3. In the figure, gray B denotes the same operating frequency zone (9.52 GHz, 10.7 GHz), in which the identity resonant frequency can be simultaneously achieved with increasing α. After the multi-optimization processing of patch length L_n for small changes and the synthesis of zones A and B, the final uniform operating frequency of the subarray over 9.8 GHz is acquired (Fig. 3(c)) when $d_1 = 0$ mm, $d_2 = 0$ mm, and $d_3 = 2$ mm; $\alpha = 17.8°$; and $L_1 = 18$ mm, $L_2 = 16.4$ mm, and $L_3 = 17$ mm. As illustrated in Fig. 3(c), the numerical reflection losses of the three elements are less than −15 dB versus −21, −15.2, and −34.8 dB. These results indicate the satisfactory impedance matching of the subarrays.

C. RADIATION PROPERTY OF ELEMENTS OF FLGA

As shown in the coordinate system in Fig. 2, the polarization axis of the elements is the y-axis. Three elements of the final optimized FLGA exhibit a special radiation property in the H-plane and E-plane (Fig. 4). The theoretical maximum radiation direction is oriented vertically toward the patch center. In the H-plane, radiation null occurs in element 1 and element 2 due to the non-uniform current distribution from the coaxial feeding line. The maximum realized gain of the two main beams of element 1 and element 2 are 0.70, 0.71, 2.7, and 2.5 dBi at angles of 35°, 143°, 38°, and 143°, respectively. The main realized gain of element 3 is 4.2 dBi at an angle of 90°. The main lobe of the first two elements below the orientation of $\varphi = 90°$ offsets a defined angle because of the wide edge effect of the trapezoidal profile of the patch. The same radiative performance is observed in

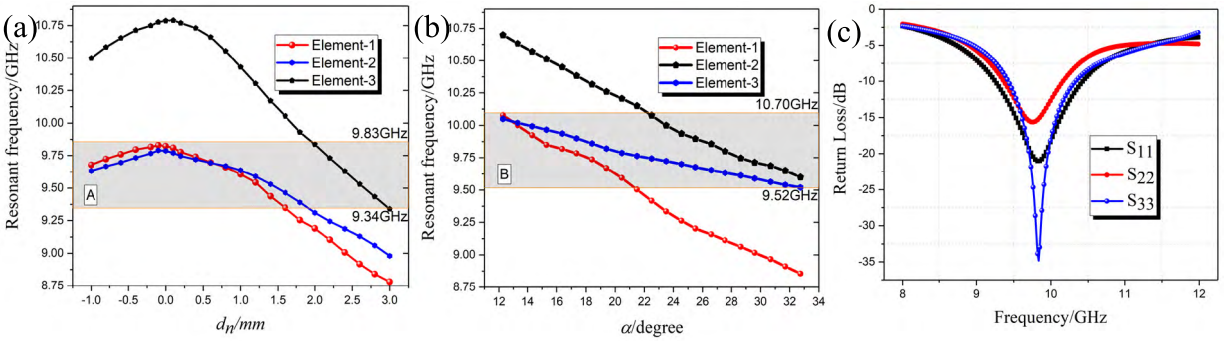

FIGURE 3. Resonant frequency referring to matching position and patch arc length when the lengths of the three elements (1–3) are 18, 16.4, and 17 mm. (a) Resonant frequency change versus d_n (the distance between the coaxial port and the patch center) when $\alpha = 17.8°$. (b) Resonant frequency change versus α (arc length of the patches wrapped around the conical surface) when $d_1 = 0$ mm, $d_2 = 0$ mm, and $d_3 = 2$ mm. (c) Final optimal return losses of three elements.

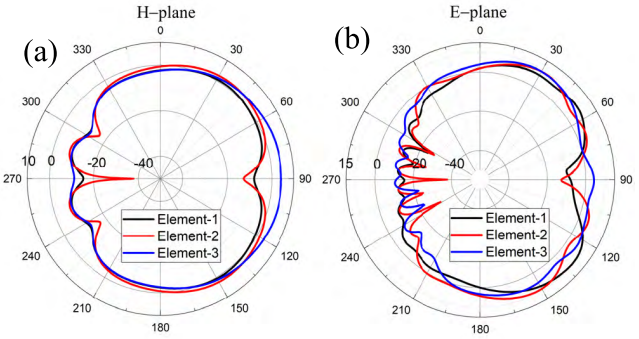

FIGURE 4. Simulated radiation pattern of three elements of the optimized FLGA at 9.8 GHz band. (a) Radiation pattern in the H-plane. (b) Radiation pattern in the E-plane.

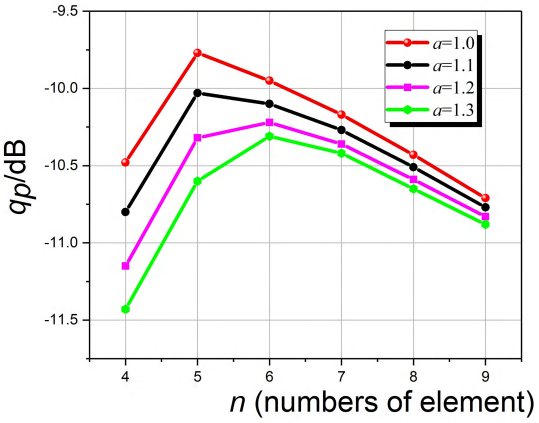

FIGURE 5. Schematic of normal performance of omnidirectional coverage with changes in element quantity.

the E-plane. However, every element reflects high numerical gains of 6.6, 8.9, and 8.2 at angles of 29°, 32°, and 30°, respectively.

III. DESIGN OF CONICAL CONFORMAL ARRAY ANTENNA

A. THEORY OF 3D RADIATION PATTERN SYNTHESIS

Conical surface characteristics that limit conformal array modification reduce the circumferential scanning angle when the number of elements increases as a result of the scanning angle of the conformal array being below ±60° [29]. If conformal antennas utilize a curved array with 360° coverage, the necessary number of circular elements should exceed 3 [29]. However, an increase in the number of arrays for fabricating the final antennas is not economical. Given the need for a conformal antenna with a wide coverage and low cost, the realized gain of the conical conformal array with an efficient radiative area based on IEEE standards is calculated as Gain $=\eta \mathrm{Dir} = 4\pi\eta A_{eff}/\lambda_0^2$, where

$$A_{eff} = \pi r l \sin\frac{2\pi}{n} \tag{3}$$

where η denotes the efficiency element radiation, r is the bottom radius, l represents the generatrix length of the cone, and n is the number of elements on R#X. A large number of elements definitely increase system cost, and scanning allows the modification of the impact of gain reduction along with a decreasing scanning angle. Hence, one performance index of an effective antenna aperture that divides the quantity of elements is proposed to denote the normal cost performance, in which

$$q_p = \frac{A_{eff}/\lambda d_l}{n} = \frac{(\cos\frac{\pi}{n})^a}{n(1+\sin\frac{\pi}{n})} \tag{4}$$

where a is the increasing mismatch loss level when the main lobe deviates from the normal orientation and d_l is the distance of the element along the generatrix direction. The implementation of cost performance through a representation of Formula (4) in MATLAB is shown in Fig. 5. The results indicate that the conformal antenna system achieves the optimal cost performance when the number of elements is 5.

Additionally, the CCAA can be considered as a narrow cylinder with multiple layers stacked one by one [14]. The radiation pattern synthesis is computed from a linear array (Fig. 6 (a)) to a circular array (Fig. 6 (b)) and conical array (Fig. 6(c)). Despite the omnidirectional coverage in the elevation plane, endfire radiation is still needed in blind

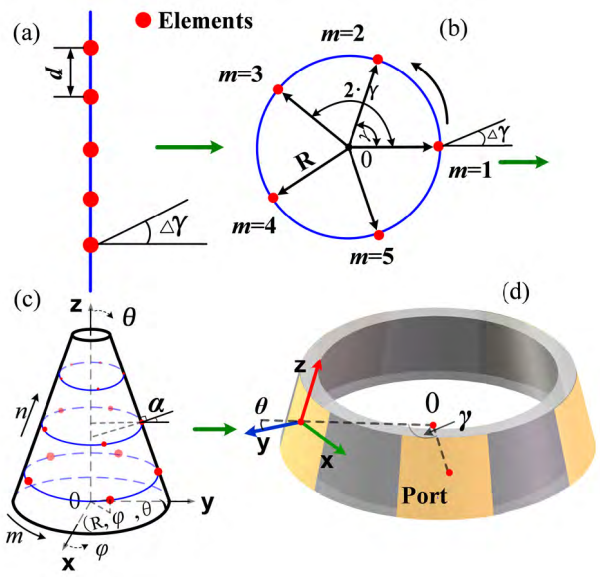

FIGURE 6. Analysis of synthesized radiation pattern for CCAA from linear array to circular array, cylinder array, and conical array. (a) Linear array of five elements whose distance between adjacent elements is d. (b) Five elements with the interval of 72° around the periphery. (c) Distribution of conformal array elements mounted on the geometrical conical surface. (d) Real conical model in the computing software.

detection. We assume that the radiated E-field expression of one element located at $\varphi = 0°$ is $\vec{E}_{u0}(\theta, \varphi) = \vec{E}^{x}_{u0}(\theta, \varphi) + \vec{E}^{y}_{u0}(\theta, \varphi) + \vec{E}^{z}_{u0}(\theta, \varphi)$, and we ignore the inter-coupling between elements. Hence, the E-fields of the m th elements can be expressed as Formula (5) by rotating $\vec{E}_{u0}(\theta, \varphi)$ at an angle of $m\gamma$, as shown in Fig. 6(d).

$$\begin{aligned}
\overrightarrow{E^{x}_{um}}(\theta, \varphi) &= \overrightarrow{E^{x}_{u0}}(\theta, \varphi + m\gamma)\cos(m\gamma) \\
&\quad + \overrightarrow{E^{y}_{u0}}(\theta, \varphi + m\gamma)\sin(m\gamma) \times \overrightarrow{z} \\
\overrightarrow{E^{y}_{um}}(\theta, \varphi) &= \overrightarrow{E^{x}_{u0}}(\theta, \varphi + m\gamma)\sin(m\gamma) \times \overrightarrow{z} \\
&\quad + \overrightarrow{E^{y}_{u0}}(\theta, \varphi + m\gamma)\cos(m\gamma) \\
\overrightarrow{E^{z}_{um}}(\theta, \varphi) &= \overrightarrow{E^{z}_{u0}}(\theta, \varphi + m\gamma)
\end{aligned} \tag{5}$$

Through endfire radiative synthesis, the three-dimensional radiation E-field of the conformal circular array can be expressed as

$$\overrightarrow{E}_{t}(\theta, \varphi) = \sum_{m=1}^{M} \left[\overrightarrow{E}_{um}(\theta, \varphi) a_m e^{jm\psi_m + jkr_m} \right] \tag{6}$$

where a_m is the feeding amplitude and ψ_m is the feeding phase difference. r_m denotes the radius of the circle where the patch feeding center is located. $k = 2\pi/\lambda$ is the free-space wavenumber.

A MATLAB program based on (5) and (6) is operated to characterize the radiation fields of the array on R#X with $a_m = 1$ and $m = 5$. By optimizing the phase difference in a solid zone $(0 - \pi)$, the optimal ψ_m is suitable in $30° - 90°$ to obtain a desirable endfire radiation.

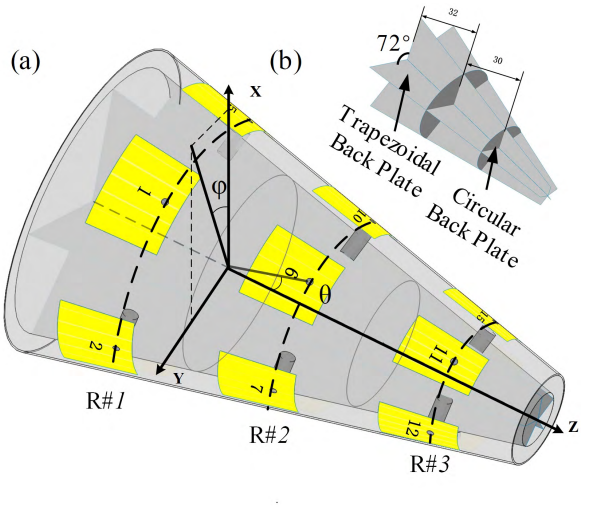

FIGURE 7. (a) 3D model configuration of the conical conformal array antenna in electromagnetic simulation software. (b) Structure of pyramid reflective back-cavity.

B. DESIGN OF CONICAL CONFORMAL ARRAY ANTENNA

The CCAA embedded within the PRBC comprises five FLGAs with a uniform circumferential arrangement (Fig. 7(a)). The PRBC is composed of five uniform trapezoidal and two circular copper plates (Fig. 7(b)). The whole CCAA is divided into 15 parts, each of which corresponds to one independent element. Each element is located on top of each part. Two circular back copper plates are in the middle of two adjacent patches of one linear subarray. Each trapezoidal copper plate is in the middle of two adjacent patches in the circumferential direction. Every element of the CCAA can be activated independently by the coaxial feeding ports for the configuration of the amplitude and phase. The elements are labeled as elements 1–15 along with the counter-clockwise as the illustration from the bottom to top of the cone.

C. SUPPLEMENTARY IMPLEMENTATION OF PHASE TO R#X

To achieve a fixed phase difference for the elements of *R#X*, we propose a 5-bit digital phase shifter in the X-band (Fig. 6). This digital phase shifter can provide multi-phase states for the output, including (0°, 11.25°), (0°, 25°), (0°, 45°), (0°, 90°), and (0°, 180°). The elements of the phase difference versus 11.25°, 25°, and 45° are implemented by loading methods. The pin-dioxide switch method is applied to 90° and 180° phase differences. The configuration of the phase shifter through a cascading connection to five elements is achieved. The total number of states is $25 = 32$. The positive biased circuits of the 25° and 45° elements are activated to obtain a 70° phase difference instead of opening other elements. With this method, a solid phase increment near 72° between two adjacent elements of R#X is achieved. The DC-bias circuit provides DC-power input and continued logic control signals to control the power switch, which is integrated at the back of the final boards. The DC control input provides voltages

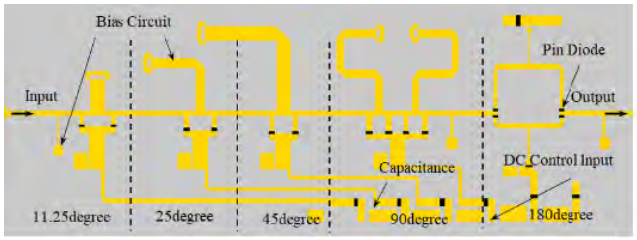

FIGURE 8. Schematic of a 5-bit digital phase shifter working in the X-band.

of ±5 and 0 V for the pin dioxide to switch over the different working states of the phase shifter. The detailed prototype and measurement process are exhibited in Part IV-A.

D. ANALYSIS OF S-PARAMETER FOR CCAA

The main consideration in maintaining the uniformity of elements of the CCAA is to maintain the same operating frequency and high isolation. After assembling the PRBC within the cone, three elements of subarray are simulated to exhibit reflective coefficients, as shown in Fig. 9. The return loss of element 6 (Fig. 7) is defined as $S_{6,6}$, that for element 11 is defined as $S_{11,11}$, and so on. The resonant frequency of the three elements are 9.84, 9.83, and 9.89 GHz with respect to return losses of −32.8, −17.2, and −40.4 dB, respectively. A slight discrepancy exists between the elements of the FLGA and the CCAA due to the reflective effect of the PRBC.

A severe mutual coupling effect deteriorates the radiation efficiency of the CCAA, especially from proximity element-3. The circumferential arrays at the bottom, at the middle, and on top of the conical surface are defined as R#*1*, R#*2*, and R#*3* for convenience. As a result of the divided spacing of the conical back-cavity, each element's electronic function is enhanced up to the radiative effect. Given the revolution symmetry of the conical structure, computing the proximity elements of one subarray and R#*X* is favorable. The simulated and measured mutual coupling coefficients are shown in Fig. 8. The illustrations in Figs. 10(a), (b), (c), and (d) correspond to the elements of the subarray and R#*X*. The overall mutual coupling coefficients between elements are less than −20 dB across all bands. As a result of the limited available space near the conic node, the width of the five elements of R#*3* is relatively narrow, resulting in a strong mutual coupling among the five elements (Fig. 10(d)). Manufacturing errors and inaccurate alignment are observed between the PSU ground and the PRBC. Hence, the measured results are not entirely agreeable with the simulated data. Nevertheless, mutual coupling tested under −20 dB indicates low EMI among different elements. This outcome indicates that no invalid radiation exists between a deactivated antenna and the source of interference.

E. ENDFIRE RADIATION PERFORMANCE OF CCAA

The main polarization direction of a planer microstrip antenna or Yagi patch antenna is usually defined along the

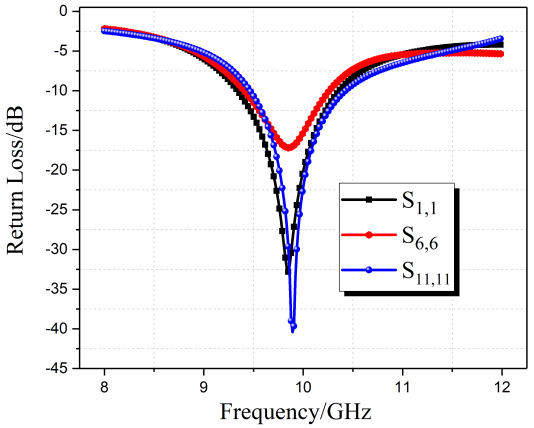

FIGURE 9. Simulated return loss of linear gradient array elements of the CCAA in the generatrix direction.

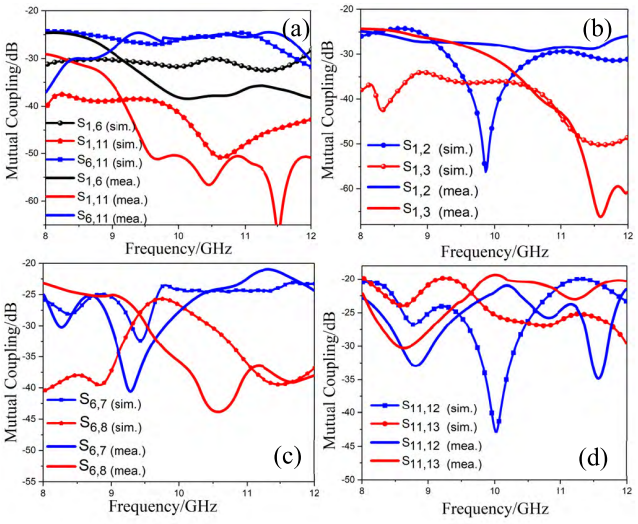

FIGURE 10. Simulated and tested mutual coupling coefficients between elements of the CCAA. (a) Elements of subarray. (b) Elements on R#1. (c) Elements on R#2. (d) Elements on R#3.

normal direction of the antenna's horizontal plane or patch arrangement path direction, respectively. Hence, the emergence of an expansive blind space can be attributed to an invalid assembly area. A possible solution is phase manipulation technology for antennas.

The five ports of R#*X* are excited with the same amplitude (1 W) and fixed phase difference (72°) between two adjacent elements (i.e., 0°, 72°, 144°, 216°, and 288°) and by replacing the metal ground with the PRBC. The numerical results of the 3D radiation pattern of different R#*X* arrays at 9.8 GHz is shown in Fig. 11. The detailed performance of R#*X* radiation is provided in Table 1. As a result of the lateral and back reflective effects of the trapezoidal copper plates and circular copper plate, both possibly provide a refractive deflective function down the cone along the $-z$ -axis in an efficient manner. The main radiation direction illustrated in Figs. 11(a), (b), and (c) is pointing toward the

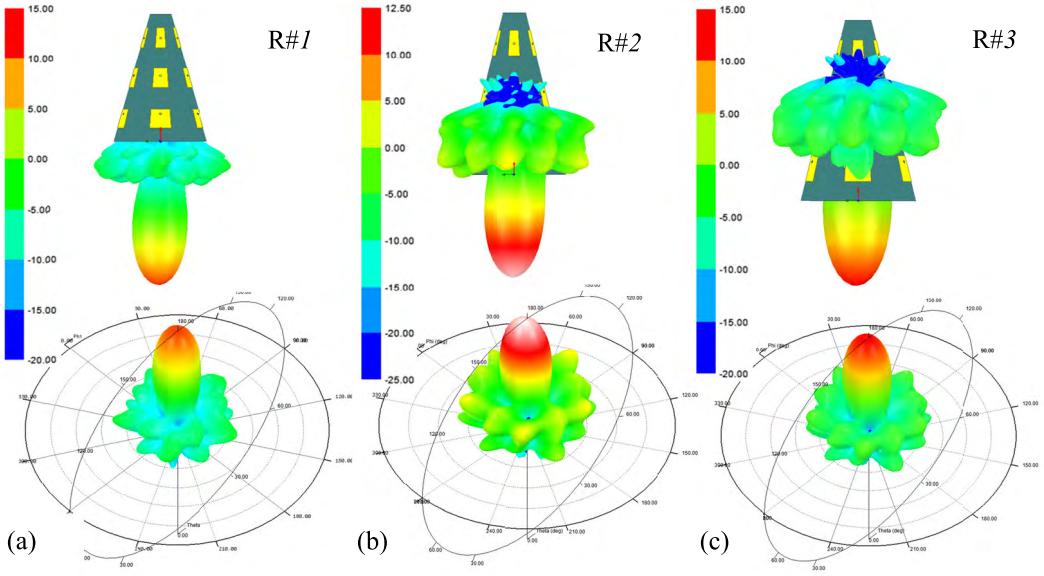

FIGURE 11. Endfire radiation of CCAA at the resonant frequency. (a), (b), and (c) 3D radiation patterns when the five elements of R#*X* (1,2,3) are excited with an identical power of 1 W and phase differences of 0°, 72°, 144°, 216°, and 288° at 9.8 GHz.

TABLE 1. R#*X* radiation parameters at 9.8 GHz.

Array	HPBW (degree)	Realized Gain (dBi)	Efficiency (%)	Radiated Power (W)
R#*1*	19.7	12.7	86.9	4.0
R#*2*	21.3	12.1	82.4	3.87
R#*3*	22.3	13.2	88.7	4.12

back endfire direction of the cone. The realized maximum gains of R#*1*, *2*, and *3* respectively reach 12.7, 12.1, and 13.2 dBi. Their efficiency levels, especially the three narrow HPBWs of 19.7°, 21.3°, and 22.3°, are 86.9%, 82.4%, and 88.7%, respectively. Moreover, their side lobe level (SLL) and back lobe level are reduced to less than −5 dBi of R#*1* and *3*; the SLL of R#2is depressed to less −2dBi. This result shows that the CCAA aided by a power divider and phase shifter that radiate the beam to the endfire direction for blind space detection in the platform, in addition to the narrow main beam, is conducive to remote scouting without interference from external factors.

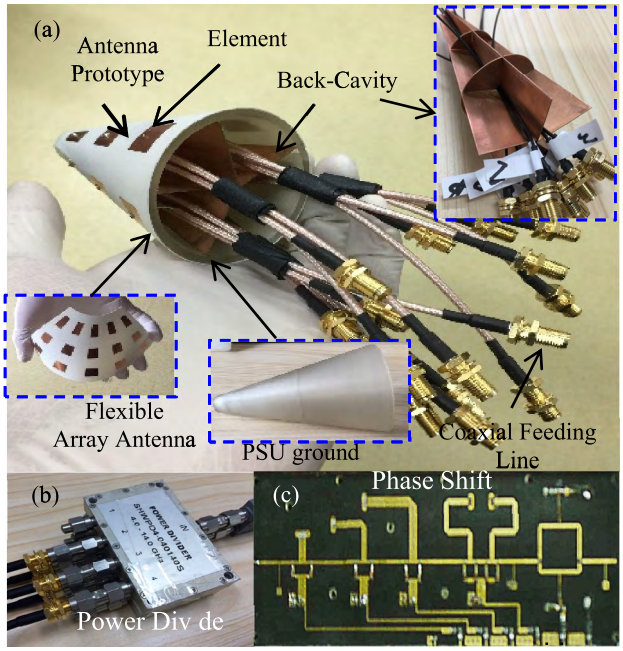

FIGURE 12. Manufactured prototype and measured supplementary components. (a) Conformal antenna prototype. (b) Power divider. (c) Phase shifter.

IV. ANTENNA FABRICATION AND MEASUREMENT FOR CONICAL CONFORMAL ARRAY ANTENNA

A. PROTOTYPE FABRICATION AND MEASUREMENT

The antenna prototype with a seamless assembly of flexible arrays and antenna-supported layers was fabricated in this study (Fig. 12). A standard PCB process and 3D polymeride printing technology are applied to manufacture the flexible array antenna and the array-supported layer, respectively. The flexible array antenna wrapped around the PSU model by plastic screws was printed on a slightly hard dielectric layer of Rogers4350. Every element was soldered with an independent coaxial feeding line. Each copper plate fabricated via laser ablation was evenly assembled on the back-cavity embedded within the PSU cone. In addition, trapezoidal copper was placed at the middle of two adjacent elements of R#*X*, with this location fixed to become a relative position configuration. In this process of fabrication, the precise assembly

TABLE 2. Elements' radiation parameters of the subarray at 9.8 GHz.

P_x	Max-Gain(H-plane)		Max-Gain(E-plane)		Tested HPBW in H-plane/°
	Sim./dBi	Mea./dBi	Sim./dir	Mea./dir	
1	5.63	4.1	8.2dBi/112°	8.53dBi/116°	37–144°
6	7.0	5.64	7.96dBi/104°	9.81dBi/109°	19–162°
11	6.85	6.0	7.0dBi/102°	7.10dBi/111°	10–172°

for the array antenna and the location of the back-cavity is difficult to achieve. To test the endfire radiation of the CCAA, we applied the power divider (model SHPDW4-040140S, Fig. 10(b)) and 5-bit phase shifter (Fig. 10(c)) fabricated by the PCB process.

In the measured process, the elements' S-parameters were tested by a vector network analyzer (Agilent N5224A). This device was used only when one element was being tested to obtain the S-parameter. Meanwhile, the other ports of the elements were loaded with 50 ohm. In this way, the other S-parameters can be obtained successively. Their radiation patterns were also tested individually at the working frequency. The input phase of the ports to R#*X* was obtained with the 5-bit phase shifter radiation pattern. The circumferential arrays connected to the power divider were tested in a standard anechoic chamber.

B. MEASUREMENT OF ELEMENTS' REFLECTIVE COEFFICIENTS

Given the revolution symmetry of the conical structure along its axis, the reflective coefficients of the three elements of one of the generatrix subarrays were measured, and the results are shown in Fig. 13. The measured and simulated operating frequency remained at 9.84 GHz. The tested working bands under −10 dB were 0.97 GHz [9.31–10.28 GHz], 0.84 GHz [9.4–10.24 GHz], and 0.94 GHz [9.47–10.41 GHz] for elements 1, 6, and 11, respectively. The measured reflective coefficients greatly agree with the simulation. A slight discrepancy in the measured return losses may be attributed to a seam slightly between the flexible array and the conical surface in the fabricated process. As shown in Fig. 14, the E-field pattern of the three elements at 9.84 GHz was distributed at a square with an area of $\lambda_0 \times 2.6\lambda_0$. The areas with strong E-fields of elements 1 and 3 were outline edges, whereas the strong E-field of element 2 merely occurred at the bottom and top edge. This result denotes that the bandwidths of elements 1 and 3 are wider than that of element 2. Furthermore, the independent operating E-field of the three elements has lower coupling interference to exhibit their high isolation. Moreover, it generates a reliable working independence in favor of the CCCA with a high operating efficiency.

C. OMINDIRECTIONAL COVERAGE OF ELEMENTS' RADIATION PATTERNS

By using the comparison of measured antennas in an anechoic chamber, three elements of one subarray were independently

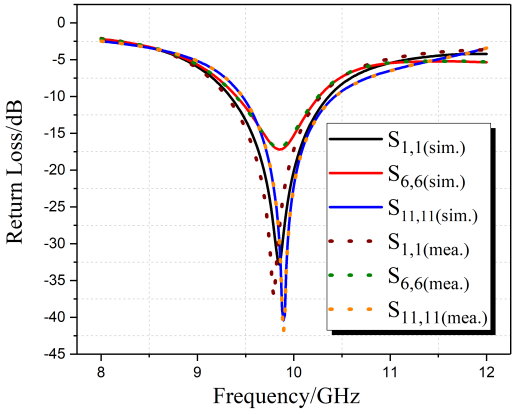

FIGURE 13. Measured and simulated reflective coefficients of elements.

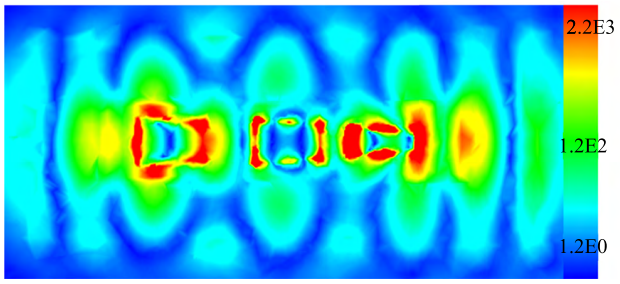

FIGURE 14. Three elements' E-field (V/m) pattern at 9.8 GHz.

activated one by one. Moreover, the radiation characteristics were formulated by comparing them with those of a 15 dBi gain standard horn antenna. The plane of $\theta = 90°$ is the H-plane, and the plane of $\varphi = 90°$ is the E-plane serving as the polarization axis along the generatrix direction. The simulated and measured radiation patterns of the three elements at 9.8 GHz in the H-plane and E-plane are shown in Fig. 15. The radiation features at 9.8 GHz in E and H-plane are summarized in Table 2. The main beam of the elements was directed to $\varphi = 90°$ in the H-plane. The minimal depression was reflected by the PRBC reflective effects. Moreover, the realized gain was higher than that of the FLGA without PRBC in the main beam direction. In addition, the tested HPBWs of the three elements in the H-plane were about 107°, 143°, and 162°. Moreover, all simulated and measured maximum gain data in the E-plane were over 7 dBi, with the maximum being 9.81 dBi. The direction of all main beams in the E-plane tilts to the direction of $\theta = 110°$ approximately because of the wide radiative side effect. To achieve an omnidirectional coverage for the peripheral array, we tested the solid angle ($\geq 72°$) scanning of R#*1* (Fig. 16). The independent radiation of each element exhibited the HPBW (3 dB band), which obviously covered the total H-plane, as indicated by the orange portion in Fig. 16. The measured discrepancy of the different elements was attributed to a fabrication error. This result shows that circumferential arrays either achieve a wide scanning angle by switching ports or they do not.

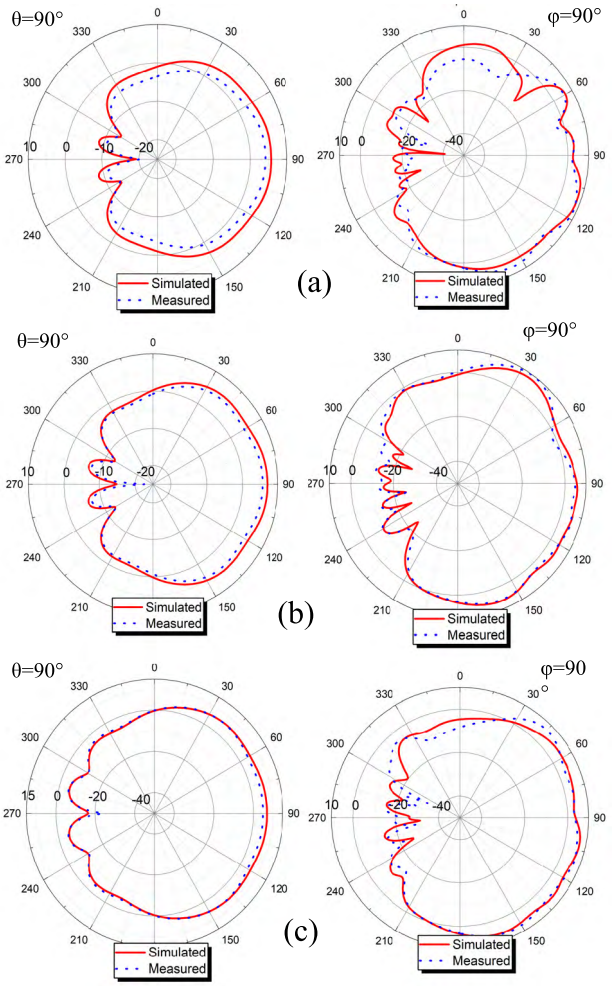

FIGURE 15. Radiation patterns of s imulated and measured elements in $\theta = 90°$ plane and $\varphi = 90°$ plane at 9.8 GHz. (a), (b), (c) versus elements 1, 2, and 3, respectively.

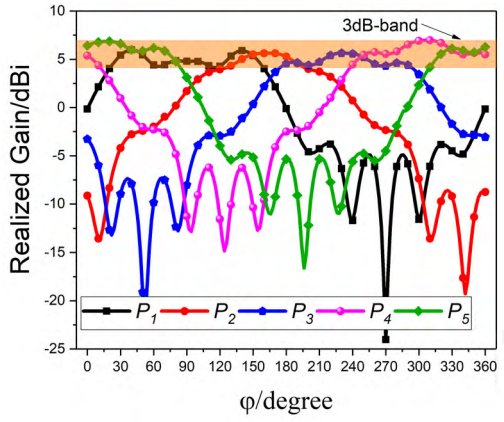

FIGURE 16. Wide solid scanning (by realization of a different patch of R#1) of omnidirectional coverage of R#1's measured radiation pattern in the $\theta = 90°$ plane at 9.8 GHz.

These arrays facilitate point-to-point communication or omni-directional radiation in the H-plane with reduced adverse scattering.

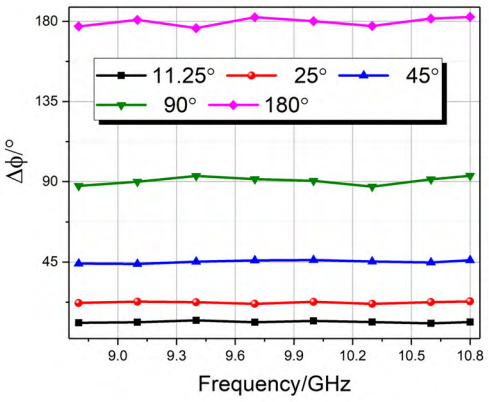

FIGURE 17. Measured phase shift accuracy of fabricated phase shifter.

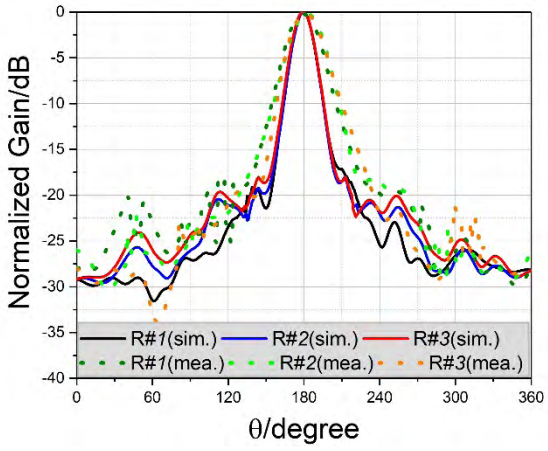

FIGURE 18. Simulated and measured radiation patterns in the E-plane when R# X is excited with the same power and phase difference of 72°.

D. RADIATION PATTERN MEASUREMENT OF R#X BY FEEDING PHASE MANIPULATION

When R#X s were tested in turn, each element connected with a phase shifter, which was activated by one of the ports of the power divider. Five ports served as activated sources fed to the elements, whereas the other ports of the power divider were sorted during measurement. The data ($\Delta\varphi$) accuracy of the phase shifter is shown in Fig. 17 through a VAN phase analysis. When $\Delta\varphi = 90°$, the maximum value of the error difference is about $\pm 3°$. In other cases, the value is lower than 3° to maintain a balance among the prediction results. The measured and co-simulated normalized gains of the radiation pattern in the E-plane are shown in Fig. 18. The co-simulation was conducted with the HFSS and ADS software. Owing to the error from the fabrication of the prototype and actual phase shift (70°) under 72°, the measured HPBW was wider than the simulated one was. The measured maximum realized gains were 10.7, 11.8, and 12.0 dBi. All these gains pointed to the $-$z-axis endfire direction of the cone. The HPBWs for R#1, R#2, and R#3 were 27.5°, 24.5°, and 26.7° in the E-plane, respectively. The corresponding normalized measured grating lobe levels were 18.2, $-$23.1,

−19.6 dBi. The R#X with a low side lobe level exhibited well-directed radiation and achieved high gain. As a result of the revolution symmetry of the conical structure, the radiation patterns in the H-plane and E-plane were almost uniform in the graphs. Above all, the properties of high gains and narrow HPBW of CCAA contribute to remote communication or blind detection.

V. CONCLUSION

A CCAA for point-to-point communication and backward blind space detection was investigated. On the basis of the method for optimizing the impedance matching position and keeping a high isolation, the FLGA with three elements operating at the same resonant frequency of 9.8 GHz was designed. Applying a PRBC improved the radiation null of the elements and intensified the adverse isolation between the elements. Therefore, each element was supplemented with a wide scanning solid angle to realize omnidirectional coverage in the H-plane for point-to-point communication. Finally, the antenna prototype was fabricated by a 3D printing technology and PCB process. The S-parameters and radiation properties of the elements were tested individually, and the outcome showed a significant agreement with the simulation results. Moreover, a 5-bit phase shifter was combined with an 8-way power divider test R#*X* radiation pattern. The measured data showed that the CCAA can obtain a narrow HPBW in the endfire direction of the cone −z-axis. This investigation is of great significance to the integration between conformal antennas and aircraft and UAVs. With the multitask execution capability of the proposed approach, it is able to facilitate point-to-point communication and backward space detection spontaneously.

ACKNOWLEDGMENT

(Hongcheng Xu and Jianli Cui contributed equally to this work.)

REFERENCES

[1] L. Matekovits, J. Huang, I. Peter, and K. P. Esselle, "Mutual coupling reduction between implanted microstrip antennas on a cylindrical bio-metallic ground plane," *IEEE Access*, vol. 5, pp. 8804–8811, 2017.

[2] C.-H. Ahn, Y.-J. Ren, and K. Chang, "A dual-polarized cylindrical conformal array antenna suitable for unmanned aerial vehicles," *Int. J. RF Microw. Comput.-Aided Eng.*, vol. 21, no. 1, pp. 91–98, Nov. 2010.

[3] Z. Wei and Y. Junfeng, "A design of vertical polarized conformal antenna and its array based on UAV structure," *Int. J. Antennas Propag.*, vol. 2017, Oct. 2017, Art. no. 9769815.

[4] Z.-C. Hao, M. He, and W. Hong, "Design of a millimeter-wave high angle selectivity shaped-beam conformal array antenna using hybrid genetic/space mapping method," *IEEE Antennas Wireless Propag. Lett.*, vol. 15, pp. 1208–1212, Nov. 2015.

[5] H. Xu *et al.*, "Wide solid angle beam-switching conical conformal array antenna with high gain for 5G applications," *IEEE Antennas Wireless Propag. Lett.*, vol. 17, no. 12, pp. 2304–2308, Dec. 2018.

[6] Y. A. Nijsure, G. Kaddoum, N. K. Mallat, G. Gagnon, and F. Gagnon, "Cognitive chaotic UWB-MIMO detect-avoid radar for autonomous UAV navigation," *IEEE Trans. Intell. Transp. Syst.*, vol. 17, no. 11, pp. 3121–3131, Nov. 2016.

[7] L. Wang, "Study of EMC technique of airborne C 3I system computer perdiction and analysis of airborne antenna coupling interference and pattern," Telecommun. Eng., Tenth Inst. Ministry Electron. Ind., Chengdu, China, Tech. Rep. 02, 1997.

[8] F. Xu, H. Zhu, Y. Ma, and Y. Qiu, "Electromagnetic performance of a three-dimensional woven fabric antenna conformal with cylindrical surfaces," *Textile Res. J.*, vol. 87, no. 2, pp. 147–154, Jun. 2016.

[9] S. Nikolaou, M. M. Tentzeris, and J. Papapolymerou, "Study of a conformal UWB elliptical monopole antenna on flexible organic substrate mounted on cylindrical surfaces," in *Proc. IEEE 18th Int. Symp. Pers., Indoor Mobile Radio Commun.*, Sep. 2007, pp. 1–4.

[10] P.-S. Kildal and S. A. Skyttemyr, "Diffraction analysis of a proposed dual-reflector feed for the spherical reflector antenna of the Arecibo Observatory," *Radio Sci.*, vol. 24, no. 5, pp. 601–617, Sep./Oct. 1989.

[11] A. Hosseinbeig, M. Kamyab, and J. S. Meiguni, "Spherical probe-fed antennas with parasitic elements," *Electromagnetics*, vol. 33, no. 4, pp. 281–291, May 2013.

[12] V. Jaeck *et al.*, "A conical patch antenna array for agile point-to-point communications in the 5.2-GHz band," *IEEE Antennas Wireless Propag. Lett.*, vol. 15, pp. 1230–1233, Nov. 2015.

[13] F. Fernandes and D. Sundararajan, "Design, development, and fabrication of a traveling-wave antenna on a conical surface," *IEEE Antennas Propag. Mag.*, vol. 52, no. 4, pp. 106–109, Aug. 2010.

[14] Y. F. Wu and Y. J. Cheng, "Conical conformal shaped-beam substrate-integrated waveguide slot array antenna with conical-to-cylindrical transition," *IEEE Trans. Antennas Propag.*, vol. 65, no. 8, pp. 4048–4056, Aug. 2017.

[15] Y. Tao, C.-Y. Yin, and L. Han, "Analysis on spherical conformal microstrip antenna array by characteristic basis function method," *Acta Physica Sinica*, vol. 63, no. 23, Jun. 2014, Art. no. 230701.

[16] J. Ouyang, X. Luo, J. Yang, K. Z. Zhang, J. Zhang, and F. Yang, "Analysis and synthesis of conformal conical surface linear phased array with volume surface integral equation+AEP (Active Element Pattern) and INSGA-II," *IET Microw., Antennas Propag.*, vol. 6, no. 11, pp. 1277–1285, Oct. 2012.

[17] W.-T. Li, Y.-Q. Hei, and X.-W. Shi, "Pattern synthesis of conformal arrays by a modified particle swarm optimization," *Prog. Electromagn. Res.*, vol. 117, pp. 237–252, Jun. 2011.

[18] E. A. Navarro, A. Luximon, I. J. Craddock, D. L. Paul, and M. Dean, "Multilayer and conformal antennas using synthetic dielectric substrates," *IEEE Trans. Antennas Propag.*, vol. 51, no. 4, pp. 905–908, Apr. 2003.

[19] M. Jobs and A. Rydberg, "Conformal dual patch antenna for diversity based sensor nodes," *Electron. Lett.*, vol. 48, no. 6, pp. 306–307, Mar. 2012.

[20] K. Wincza, S. Gruszczynski, and K. Sachse, "Conformal four-beam antenna arrays with reduced sidelobes," *Electron. Lett.*, vol. 44, no. 3, pp. 174–175, Jan. 2008.

[21] P. Jacobsson and T. Rylander, "Gradient-based shape optimisation of conformal array antennas," *IET Microw., Antennas Propag.*, vol. 4, no. 2, pp. 200–209, Feb. 2010.

[22] H.-X. Zhou, R. Lai, S.-Q. Liu, and G. Jiang, "New improved nonuniformity correction for infrared focal plane arrays," *Opt. Commun.*, vol. 245, pp. 49–53, Jan. 2005.

[23] Y.-Y. Bai, S. Xiao, M.-C. Tang, Z.-F. Ding, and B.-Z. Wang, "Wide-angle scanning phased array with pattern reconfigurable elements," *IEEE Trans. Antennas Propag.*, vol. 59, no. 11, pp. 4071–4076, Nov. 2011.

[24] X. Ding, B. Z. Wang, and G. Q. He, "Research on millimeter-wave phased array with wide-angle scanning performance," *IEEE Trans. Antennas Propag.*, vol. 61, no. 10, pp. 5319–5324, Oct. 2013.

[25] P. J. Zarco-Tejada, V. González-Dugo, and J. A. J. Berni, "Fluorescence, temperature and narrow-band indices acquired from a UAV platform for water stress detection using a micro-hyperspectral imager and a thermal camera," *Remote Sens. Environ.*, vol. 117, no. 1, pp. 322–327, Feb. 2012.

[26] H. Sedjelmaci, S. M. Senouci, and N. Ansari, "Intrusion detection and ejection framework against lethal attacks in UAV-aided networks: A Bayesian game-theoretic methodology," *IEEE Trans. Intell. Transp. Syst.*, vol. 18, no. 5, pp. 1143–1153, May 2017.

[27] W. L. Stutzman and G. A. Thiele, *Antenna Theory and Design*. Hoboken, NJ, USA: Wiley, 1981

[28] R. J. Mailloux, *Phased Array Antenna Handbook*. Norwood, MA, USA: Artech House, 2017.

[29] L. Josefsson and P. Persson, *Conformal Array Antenna Theory and Design*. Piscataway, NJ, USA: IEEE Press, 2006.

HONGCHENG XU was born in Huanggang, Hubei, China, in 1992. He received the B.S. degree in detection guidance and control technology and the M.S. degree in instrument science and technology from the North University of China, in 2016 and 2019, respectively. He is currently pursuing the Ph.D. degree. His research interests include flexible antennas, conformal antennas, 5G antennas, and MEMS technology.

JIANLI CUI received the Ph.D. degree from the North University of China, in 2018. She is currently a Teacher with Yuncheng University, Shanxi, China. She has published many high-level scientific articles about MEMS technology, sensor principle, and flexible electric devices. Her research interests are helpful for flexible electric devices in design and manufacture.

JUNPING DUAN received the Ph.D. degree from the North University of China, in 2015, where she is currently a Professor. She has mastered a project of the National Natural Science Foundation of China and the National Defense Pre-Research Foundation of China. Her research interests include flexible antennas, THz filter, metamaterials, and waveguide slot array antenna.

BINZHEN ZHANG is currently a Professor with the North University of China, China, where he has been appointing as the Deputy Director of the Key Laboratory of Instrumentation Science and Dynamic Measurement, Ministry of Education. He has published over 100 articles in the SCI library. His remarkable scientific work has created a great progress in academic word. His research interests include functional materials, nano-materials, MEMS, RF and microwave technology including antenna, filter, coupler, power divider, phase shifter, and amplifier.

YING TIAN is currently a Senior Researcher with Sichuan Aerospace Liaoyuan Science and Technology, Co., Ltd. Her research interests include MEMS sensor technology and fabricated technology.